Finite Volume Time Domain Room Acoustics Simulation under General Impedance Boundary Conditions

Stefan Bilbao, *Senior Member, IEEE*, Brian Hamilton, Jonathan Botts, and Lauri Savioja, *Senior Member, IEEE*

Abstract—In room acoustics simulation and virtualization applications, accurate wall termination is a perceptually crucial feature. It is particularly important in the setting of wave-based modeling of 3D spaces, using methods such as the finite difference time domain method or finite volume time domain method. In this paper, general locally reactive impedance boundary conditions are incorporated into a 3D finite volume time domain formulation, which may be specialized to the various types of finite difference time domain method under fitted boundary termination. Energy methods are used to determine stability conditions for general room geometries, under a large family of nontrivial wall impedances, for finite volume methods over unstructured grids. Simulation results are presented, highlighting in particular the need for unstructured or fitted cells at the room boundary in the case of the accurate simulation of frequency-dependent room mode decay times.

Index Terms—Finite difference time domain method, finite volume methods, room acoustics.

I. INTRODUCTION

FULL spatiotemporal simulation of acoustic wave propagation over grids, for purposes of virtual acoustic rendering, or artificial reverberation offers, at least in theory, a complete description of wave phenomena within an enclosure or room. Such methods have seen increased interest in recent years, particularly using finite difference time domain (FDTD) methods [1]–[3], and equivalent digital waveguide mesh [4], [5] formalisms. Finite volume time domain (FVTD) methods have a long history of use in applications in fluid dynamics [6] and electromagnetics [7], and were presented in the context of room acoustics as a generalization of FDTD to quasi-Cartesian grids [2], yet lacking conditions for numerical stability at boundaries. More recently, FVTD methods have been presented allowing for fully unstructured grids with energy-stable impedance boundary terminations [8].

The advantages of such direct grid-based time-stepping methods are many. Relative to standard room acoustics rendering methods such as ray tracing or the image source method [9], one advantage is the ability to handle arbitrary room shapes without simplifying geometrical assumptions, and thus simulate diffraction effects in a natural manner. Another advantage is flexibility—as the acoustic field is available in its entirety over the problem domain, applications in virtualization involving moving sources or receivers require minimal computational overhead. A third is the highly parallel nature of such algorithms, particularly when explicit methods are used, and when the grid has a regular ordering, at least over the problem interior.

A major concern in room acoustics applications is the accurate modeling of boundary conditions over an irregularly-shaped domain boundary or wall. In particular, the main feature of interest, the absorption, is highly frequency dependent, and such frequency dependence necessarily implies boundary conditions which are reactive (or capable of storing energy) and thus nontrivial to model and implement. For time-stepping methods such as FDTD or FVTD, two main issues emerge.

First is the question of numerical stability for the algorithm as a whole, for a given update over the interior, complemented by numerical boundary conditions which correspond, generally, to impedance terminations of type which may vary over the room boundary. For FDTD methods operating over Cartesian grids, frequency domain techniques such as von Neumann analysis [10], [11] give necessary stability conditions on unbounded domains or problems on bounded domains that allow for a Fourier series decomposition of spatial modes (such as, e.g. a clamped rectangular membrane). If the boundaries are of a simple type (such as, e.g., a plane aligned with the grid in one of the coordinate directions), then such analysis may be extended, as per the methods developed by Gustafsson, Sundstrom, Kreiss and Osher [12]. If, however, the grid is unstructured, either over the interior, or at the boundary, and if the boundary itself is of an irregular shape, then such frequency domain methods do not apply directly. For example, boundary models thought to be stable by frequency domain analyses [13], [14] have been found to be prone to instabilities at re-entrant edges/corners [15], [16]. The difficulties are obviously compounded when the wall condition itself is of a nontrivial form (i.e., it is characterized by a frequency-dependent reflectance, again variable over the room boundary).

Second is the question of the accuracy of the boundary condition. A standard approach, particularly when methods operating

over structured grids are employed, is to make use of a so-called staircase approximation to the boundary. Though such methods have the virtue of ease of programming, such methods suffer from a decrease in accuracy, when viewed in terms of computed mode frequencies, and also time domain artefacts, as illustrated in 2D recently in [8]. A much larger effect of using such a staircase boundary, and one that will be illustrated in this article, is that of severe inaccuracy in calculated decay times under absorptive wall conditions. On top of this, the frequency-dependent character of the impedance boundary condition requires specialized design techniques. Though some authors use an approach based on running multiple simulations over different frequency bands [17], [18], each associated with a constant wall reflectance, for the sake of efficiency it is desirable to model the frequency-dependent character of the wall conditions over the entire audio frequency range simultaneously.

Finite volume approaches constitute a useful design methodology which tackles both of the issues mentioned above. Stability analysis can be carried out in the fully unstructured case, by making use of energy methods, and allow for numerical stability conditions for complex geometries, and for simple impedance boundary conditions [8]. Furthermore, through the use of fitted cells, rather than staircase approximations at the room boundary, much better accuracy can be obtained in terms of temporal coherence of responses and mode frequencies. As mentioned above, finite volume methods generalize certain FDTD schemes on structured grids over the interior, and as such can be thought of as a means of the construction and analysis of such schemes under complex boundary termination in the fully unstructured case.

Some basic results on FVTD have been provided in [8]. The current article extends the scope of this work significantly in various ways, towards tackling real-world room acoustics problems, by introducing a general passive wall admittance formulation, suitable for fitting against theoretical or measured values, while maintaining the important energy balance property crucial in finding numerical stability conditions. In addition, whereas only full cubic cells were tested in [8], this work considers fitted cells for nontrivial 3D room geometries, as well as adaptations to dodecahedral cells for a 13-point FDTD scheme on the face-centered cubic (FCC) grid, which has been found to be more computationally efficient than conventional 27-point schemes [19]. The use of fitted cells in this study illustrates greatly improved results in terms of calculated T_{60} times relative to simple staircase approximations.

In Section II, the model equations for linear acoustics are given, for a general room geometry, accompanied by locally-reactive boundary conditions of a general form, described in a multi-branch circuit form, and an energy analysis illustrating the passivity of the combined initial/boundary value problem. (Passivity here means that, for an initial value problem, the total stored energy of the room, including the walls, must be non-increasing over time.) Finite volume discretization is outlined in Section III, as well as the specialization to Cartesian and FCC grids, in which case such methods are equivalent to known finite difference time domain methods. The distinction between staircase and fitted cell approximations is discussed, with reference in particular to convergence of such approximations in volume and the bounding area. Discrete time approximations are introduced in Section IV, leading to convenient global numerical stability conditions, obtained through energy analysis. The determination of model parameters from nontrivial absorptive materials is covered in Section V. Finally, in Section VI, various illustrations of the accuracy of such fitted approximations relative to staircase approximations are provided under a variety of boundary conditions for some representative geometries, highlighting especially the gross inaccuracy in calculated T_{60} times under staircase boundary termination. The strict numerical energy conservation and dissipation properties of such schemes are also illustrated.

II. MODEL EQUATIONS

A model of the dynamics of an acoustic field within an enclosure is given by the following system:

$$\frac{1}{\rho c^2}\frac{\partial p}{\partial t} + \nabla \cdot \mathbf{v} = 0 \tag{1a}$$

$$\rho\frac{\partial \mathbf{v}}{\partial t} + \nabla p = \mathbf{0}. \tag{1b}$$

Here, $p = p(\mathbf{x}, t)$ and $\mathbf{v} = \mathbf{v}(\mathbf{x}, t)$ are the pressure and particle velocity, respectively; both are functions of time $t \in \mathbb{R}^+$ and a spatial coordinate $\mathbf{x}$. In particular, $\mathbf{x} \in \mathcal{V} \subset \mathbb{R}^3$, where $\mathcal{V}$ is the room enclosure. The physical constants ρ and c are the density of air and wave speed in air, respectively, and in this work take the constant values $\rho = 1.21\ \text{kg} \cdot \text{m}^{-3}$ and $c = 340\ \text{m} \cdot \text{s}^{-1}$. ∇ and $\nabla\cdot$ are the three-dimensional gradient and divergence operations, respectively. System (1) must be complemented by two initial conditions $p(\mathbf{x}, 0) = p_0(\mathbf{x})$ and $\mathbf{v}(\mathbf{x}, 0) = \mathbf{v}_0(\mathbf{x})$; in this article, it is assumed that the system is unforced, so only the initial/boundary value problem is considered.

System (1) may be written in a second order form,

$$\frac{\partial^2 \Psi}{\partial t^2} = c^2 \nabla^2 \Psi, \tag{2}$$

using a velocity potential $\Psi = \Psi(\mathbf{x}, t)$, [20], defined by

$$p = \rho\frac{\partial \Psi}{\partial t}, \mathbf{v} = -\nabla\Psi, \tag{3}$$

and where $\nabla^2 = \nabla \cdot \nabla$ is the Laplacian.

The model (1) above is simplified from the linearized Navier Stokes equations [20], where $\mathbf{v}$ is the irrotational part of the velocity vector field, and where viscothermal loss effects have been neglected. This model, or more commonly the second order form (2), is the starting point for most wave based simulations of room acoustics. Generalizations to include effects of viscothermal damping, important in modeling wave propagation in large enclosures, will not be addressed here. See, e.g., [21], [22].

A. Energy Balance

A total energy balance for system (1) may be derived [8] as

$$\frac{d\mathcal{H}_i}{dt} = -\mathcal{B}, \tag{4}$$

where the total energy $\mathcal{H}_i(t)$ stored in the acoustic field is defined by

$$\mathcal{H}_i = \int\int\int_{\mathcal{V}} \frac{\rho}{2}|\mathbf{v}|^2 + \frac{1}{2\rho c^2}p^2 dV \geq 0, \tag{5}$$

where dV is a differential volume element, and where $\mathcal{B}(t)$, a boundary term resulting from an application of Gauss's theorem, is given by

$$\mathcal{B} = \int\!\!\int_{\partial\mathcal{V}} p v_{\perp} \, d\sigma. \qquad (6)$$

Here, $\partial\mathcal{V}$ is the boundary of the room volume $\mathcal{V}$, with outward normal $\mathbf{n}$, and where $v_{\perp} = \mathbf{n} \cdot \mathbf{v}$ is the normal component of the particle velocity over the boundary, with $d\sigma$ as a differential surface element.

B. Impedance Boundary Conditions

An obvious requirement of any wall condition in a room acoustics setting is passivity—the wall material may be capable of storing or dissipating (but not generating) energy. Considering the energy balance given in (4), it then follows that for passivity, it must be true that

$$\mathcal{B} = \mathcal{Q} + \frac{d\mathcal{H}_{\mathrm{b}}}{dt} \quad \text{with} \quad \mathcal{Q} \geq 0 \quad \text{and} \quad \mathcal{H}_{\mathrm{b}} \geq 0, \qquad (7)$$

where $\mathcal{Q}(t)$ represents power dissipated by the wall termination, and $\mathcal{H}_{\mathrm{b}}(t)$ the stored energy at the boundary. Under the non-negativity conditions above, it then follows that (4) may be written as

$$\frac{d\mathcal{H}}{dt} = -\mathcal{Q} \leq 0 \Rightarrow 0 \leq \mathcal{H}(t) \leq \mathcal{H}(0) \quad \text{for} \quad t \in \mathbb{R}^{+}, \qquad (8)$$

where $\mathcal{H} = \mathcal{H}_{\mathrm{i}} + \mathcal{H}_{\mathrm{b}}$ is the total energy stored in the acoustic field and at the wall. The interest of such a condition is that it may be transferred to the discrete setting, leading to sufficient conditions for numerical stability in time-stepping methods. The numerical counterpart of (8) is an invaluable design and debugging tool—under lossless boundary conditions, a properly designed scheme will exhibit numerical energy conservation to the level of accuracy of the machine ("machine epsilon"), and when losses are present, a numerical energy balance must be satisfied, whereby the cumulated power dissipated at the boundary must exactly cancel that lost in storage, again to machine accuracy.

Examining the term $\mathcal{B}$ from (6), then a locally reactive boundary condition [23] may be framed in terms of a time-differential relation between the pressure $p(\mathbf{x}, t)$ and the normal velocity component $v_{\perp}(\mathbf{x}, t)$, for $\mathbf{x} \in \partial\mathcal{V}$. It is often characterized, after introducing Laplace transformed quantities $\hat{p}(\mathbf{x}, s)$ and $\hat{v}_{\perp}(\mathbf{x}, s)$, by an admittance $Y(\mathbf{x}, s)$, where

$$\hat{v}_{\perp} = Y\hat{p}, \qquad (9)$$

and where s is the usual transform variable. Local reactivity implies that each point on the wall surface is capable of storing and dissipating energy, as well as transferring it back to the acoustic field—but that no direct energy transfer is allowed between distinct points along the wall. For passivity, the admittance $Y(\mathbf{x}, s)$ must be positive real [24] for every $\mathbf{x} \in \partial\mathcal{V}$. For time domain simulation purposes, it is rational approximations of finite order that are of interest; for such an approximation, there is always a representation in terms of a passive one-port network, which, if the form of the admittance is known, may be arrived at through conventional network synthesis procedures such as
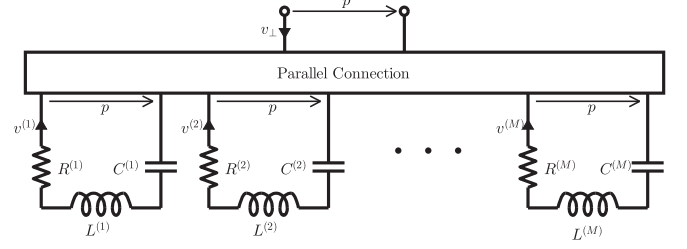

Fig. 1. One-port circuit representation of a boundary admittance, as a parallel combination of M series RLC branches.

those of Brune [25], Bott and Duffin [26], and others. See the text by van Valkenburg [27] for an overview.

In the present case, where the boundary conditions will be fitted to measured admittances, or empirical formulas, a simplified representation allowing for straightforward numerical implementation, but sacrificing some generality is of interest. One useful constraint is that the wall admittance is zero at the DC frequency, following from the observation that steady DC flow in the direction of the wall is unphysical. A one-port parallel structure, containing M series branches is shown in Fig. 1, where $v_{\perp}(\mathbf{x}, t)$ and $p(\mathbf{x}, t)$ are interpreted as the current and voltage, respectively. The mth branch is a series combination of an inductance $L^{(m)}(\mathbf{x}) \geq 0$, resistance $R^{(m)}(\mathbf{x}) \geq 0$ and finite capacitance $C^{(m)}(\mathbf{x}) > 0$; all are non-negative. The admittance of the network is

$$Y(\mathbf{x}, s) = \sum_{m=1}^{M} \frac{s}{L^{(m)}(\mathbf{x})s^2 + R^{(m)}(\mathbf{x})s + \frac{1}{C^{(m)}(\mathbf{x})}}. \qquad (10)$$

The one-port structure relates $\hat{v}_{\perp}$ and $\hat{p}$, allowing for the closure of (9). Note that for $M = 1$, the circuit representation reduces to the series combination of a mass, spring and resistance, as in simpler models of wall admittances [28]. Note also that because of $C^{(m)}(\mathbf{x}) > 0$, the condition of zero admittance at DC is enforced—this assumption may be relaxed if, e.g., one is interested in examining simple frequency-independent loss, which is clearly an idealization, though a very useful one.

Writing $v^{(m)}$ as the partial current in the mth branch, in the time domain, the differential relationships between $v_{\perp}$ and p are

$$v_{\perp} = \sum_{m=1}^{M} v^{(m)} \qquad (11\text{a})$$

$$p = L^{(m)} \frac{dv^{(m)}}{dt} + R^{(m)} v^{(m)} + \frac{1}{C^{(m)}} g^{(m)} \quad (11\text{b})$$

$$\frac{dg^{(m)}}{dt} = v^{(m)}, \qquad (11\text{c})$$

for $m = 1, \ldots, M$. Note that the new variable $g^{(m)}$ has been introduced here, reflecting the integration in the capacitor—the need for such an additional variable follows from the reactive nature of the capacitance. Examining the boundary term $\mathcal{B}$ from (7), and using (11), one has

$$\mathcal{B} = \int\!\!\int_{\partial\mathcal{V}} v_{\perp} p \, d\sigma \overset{(11\text{a})}{=} \sum_{m=1}^{M} \int\!\!\int_{\partial\mathcal{V}} v^{(m)} p \, d\sigma$$

$$\overset{(11\text{b})(11\text{c})}{=} \mathcal{Q} + \frac{d\mathcal{H}_{\mathrm{b}}}{dt}, \qquad (12)$$
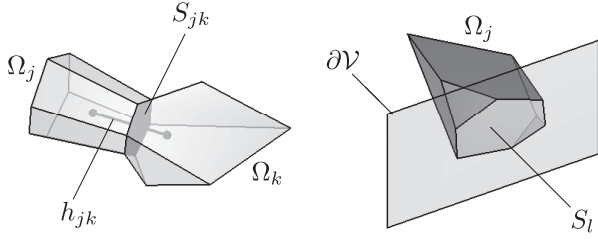
Fig. 2. Left: two irregular polyhedral cells Ω_j and Ω_k, with an adjoining face, of surface area S_{jk}, and with inter-cell distance h_{jk}. Right: a cell Ω_j with a boundary face, of surface area S_l.
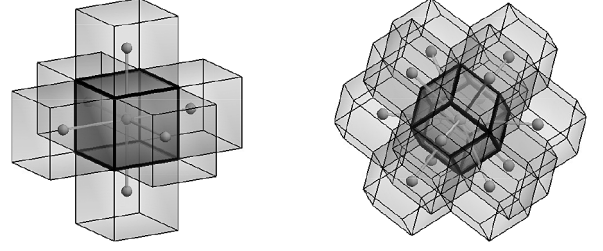

Fig. 3. Cells surrounded by their nearest neighbors and stencil of points used in equivalent finite difference scheme: Left, a cubic cell (cubic grid), and right, a rhombic dodecahedral cell (FCC grid).

where

$$Q = \sum_{m=1}^{M} \int\int_{\partial V} R^{(m)} \left(v^{(m)} \right)^2 d\sigma \geq 0 \qquad (13)$$

$$H_b = \frac{1}{2} \sum_{m=1}^{M} \int\int_{\partial V} L^{(m)} \left(v^{(m)} \right)^2 + \frac{1}{C^{(m)}} \left(g^{(m)} \right)^2 d\sigma \geq 0, \qquad (14)$$

and thus the system as a whole is passive, satisfying (8).

There are obviously many other topologies which also lead to passive termination—see the comments in Section VII.

III. FINITE VOLUME METHODS

Finite volume methods for acoustic wave propagation are described in [8]. As mentioned in the introduction, such methods generalize certain finite difference time domain methods, allowing for convenient treatment of complex boundary termination ensuring numerical stability. The method will be outlined in brief below.

A. Cells and Finite Volume Formulation

The starting point in a finite volume discretization is the definition of N non-overlapping cells Ω_j, $j = 1, \ldots, N$, covering the domain of interest, here V. In general, these may be chosen as three-dimensional polyhedra. The volume of cell Ω_j is V_j; the area of the adjoining surface and the distance between cells Ω_j and Ω_k are S_{jk} and h_{jk}, respectively.[1] For a cell with a boundary on ∂V, the boundary surface area is S_l, for $l = 1, \ldots, N_b$, where N_b is the total number of boundary faces. See Fig. 2.

First, introduce pressures $p_j(t)$, representing an average pressure over the cell Ω_j, and outward normal velocities $v_{jk}(t)$ averaged over the surface adjoining cells Ω_j and Ω_k; in particular, $v_{jk} = -v_{kj}$. Through the use of Gauss's theorem, the first of system (1) may be written as

$$\frac{V_j}{\rho c^2} \frac{dp_j}{dt} + \sum_{k=1}^{N} \beta_{jk} S_{jk} v_{jk} + \sum_{l=1}^{N_b} \gamma_{jl} S_l v_l = 0, \qquad (15)$$

$\forall j = 1, \ldots, N$. Here, β_{jk} is an indicator function, taking on the value 1 if Ω_j and Ω_k share a common face, and 0 otherwise. Similarly, γ_{jl} is an indicator function selecting for a cell

[1]There is some freedom to choose inter-cell distances, but they can be uniquely determined by centroids of cells or by the nodes in a Voronoi tessellation. For boundary cells it may be desirable to choose inter-cell distances based on the centroids of boundary faces.

Ω_j which possesses a face l of surface area S_l on the outer boundary of the domain V. Such a face is associated with an outward normal velocity v_l. The second of system (1) may be approximated as

$$\rho \frac{dv_{jk}}{dt} + \frac{1}{h_{jk}} (p_k - p_j) = 0. \qquad (16)$$

B. Cell Types

In general, finite volume methods operate over unstructured collections of cells; in room acoustics simulation applications, which can require very large numbers of such cells, it is useful to employ a regular arrangement of cells over the problem interior, with some specialization of cells at the boundary. Under such conditions, finite volume updates are for the most part uniform over the domain, as in finite difference time domain methods, with the underlying finite volume formulation remaining as a tool allowing for the definitive analysis of numerical stability, and also in the determination of stable boundary conditions.

To this end, two useful cell types which tile three-dimensional space are the cubic cell and the rhombic dodecahedral cell (the Voronoi cell of the FCC grid) [19]. See Fig. 3.

If the distance between cell centers is h, then for cubic cells,

$$V_j = h^3 \qquad S_{jk} = h^2 \qquad h_{jk} = h, \qquad (17)$$

and for rhombic dodecahedral cells,

$$V_j = \frac{1}{\sqrt{2}} h^3 \qquad S_{jk} = \frac{1}{2\sqrt{2}} h^2 \qquad h_{jk} = h. \qquad (18)$$

C. Staircase Approximations and Fitted Boundary Cells

For an arbitrary domain, and if one is using a regular arrangement of cells, such as the Cartesian (cubic) or rhombic dodecahedral tilings mentioned above, then the simplest approach to terminating the computational volume is to use a staircase approximation—those cells whose centers lie within the volume of interest are retained, in their entirety. Clearly, in the limit of small cells, the volume of such an approximation approaches that of the model domain. The surface area of the domain boundary, however, does not, even in an approximate sense. See Fig. 4, illustrating staircase approximations to a spherical region using Cartesian cells—in the limit of small cell sizes, the total boundary area of the staircase region approaches 1.5 times that of the sphere itself.
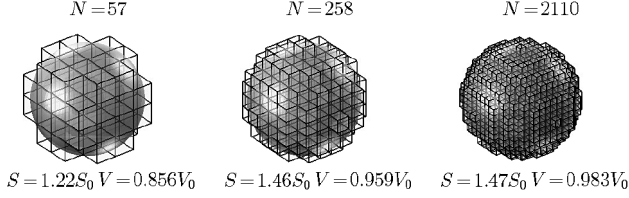
Fig. 4. Staircase approximations to a spherical region, with radius r, and of volume $V_0 = 4\pi r^3/3$ and surface area $S_0 = 4\pi r^2$, using Cartesian cells, for different numbers N of cells as indicated. The total volume and surface area of the staircased regions, relative to V_0 and S_0 are indicated in each case.
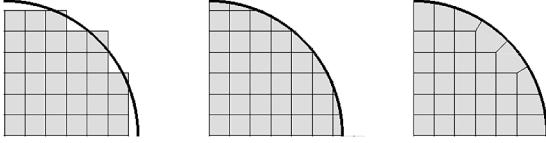

Fig. 5. Staircase and fitted approximations in 2D, using Cartesian cells. Left: staircase approximation. Centre: One possible fitted-cell tiling. Right: An alternative tiling illustrating more uniform cell volumes.

In some settings in computational room acoustics, such as, e.g., the case of perfectly reflecting wall conditions, the numerical surface area of the room boundary does not intervene explicitly, and one should expect, in a simulation, that room modal frequencies should approach those of the model problem. If, as in the case of realistic wall impedances incorporating the effects of loss, the total surface area is significant, then one should expect that such a staircase approximation should lead to significant error. In practice, and as will be illustrated in Section VI, the effect can be a gross distortion of the decay times within the room—and one which does not disappear even in the limit of very small cells, or, equivalently, high sampling rates.

To this end, the use of a regular arrangement of cells over the domain interior, with an adjustment to cells at the boundary is of great use—not only are modal frequencies calculated to greater accuracy, but as the surface area of such a collection of fitted cells will indeed converge to that of the model domain, the numerically calculated decay times will also approach correct values in the limit of small cell size. See Fig. 5 for an illustration of Cartesian cells fitted to an irregular boundary (shown in 2D, for the sake of visibility).

IV. TIME DISCRETIZATION

Suppose the ODE system (15)–(16) is to be discretized with time step T_s, where $F_s = 1/T_s$ is the sampling rate. Define p_j^n and $v_{jk}^{n+1/2}$ to be interleaved approximations to $p_j(t = nT_s)$ and $v_{jk}(t = (n+1/2)T_s)$, respectively, for $j, k = 1, \ldots, N$.

Define the forward and backward shift operators e_+ and e_-, for a time series f^n, where n is either integer or half integer, as

$$e_+ f^n = f^{n+1}, e_- f^n = f^{n-1}. \quad (19)$$

One can then define both forward and backward difference operators δ_+ and δ_- as:

$$\delta_+ = \frac{1}{T_s}(e_+ - 1), \delta_- = \frac{1}{T_s}(1 - e_-). \quad (20)$$

A fully discrete formulation of system (15)–(16) is then

$$\frac{V_j}{\rho c^2}\delta_+ p_j + \sum_{k=1}^{N}\beta_{jk}S_{jk}v_{jk} + \sum_{l=1}^{N_b}\gamma_{jl}S_l v_l = 0 \quad (21a)$$

$$\rho\delta_- v_{jk} + \frac{1}{h_{jk}}(p_k - p_j) = 0. \quad (21b)$$

Here, time indices have been suppressed—every instance of a time series p (respectively v) is assumed evaluated at time step n (respectively $n + 1/2$). Notice that the updates (21b) may always be evaluated explicitly, as may (21a) at cells Ω_j which do not possess a boundary face. Note that the pressure and velocity variables in scheme (21) above are thus interleaved, and the use of two distinct operators δ_+ and δ_- is for convenience.

Using $p_j = \rho\delta_-\Psi_j$, for some discrete velocity potential $\Psi = \Psi_j^{n+1/2}$, a second order form for system (21) may be written as

$$\delta_+\delta_-\Psi_j + \frac{c^2}{V_j}\sum_{k=1}^{N}\frac{\beta_{jk}S_{jk}}{h_{jk}}(\Psi_j - \Psi_k) + \frac{c^2}{V_j}\sum_{l=1}^{N_b}\gamma_{jl}S_l v_l = 0. \quad (22)$$

When specialized to regular arrangements of cells, such as Cartesian or rhombic dodecahedral, such a scheme is familiar as a two-step FDTD scheme.

A. Energy Balance

At this stage, it is possible to arrive at an energy balance analogous to (4). Finite volume methods are often referred to as conservative in the literature [6]—flux conservation laws across cell boundaries are preserved. Here, the idea is to conserve a global scalar energy-like quantity. To this end, it is useful to define the averaging operator μ_+ as

$$\mu_+ = \frac{1}{2}(e_+ + 1), \quad (23)$$

and to note the following identities and inequalities involving products of time series under the action of difference and averaging operations:

$$(\mu_+ f)(\delta_+ f) = \delta_+\left(\frac{1}{2}f^2\right)$$

$$(\mu_+\delta_- f)(f) = \delta_+\left(\frac{1}{2}fe_- f\right) \quad (24)$$

$$fe_- f \geq -\frac{T_s^2}{4}(\delta_- f)^2. \quad (25)$$

Multiplying (21a) by $\mu_+ p_j$, summing over all cells, making use of identities (24) and employing (21b), leads to the discrete time energy balance

$$\delta_+\mathfrak{h}_i = -\mathfrak{b}, \quad (26)$$

which is analogous to (4), and where

$$\mathfrak{h}_i = \sum_{j=1}^{N}\left(\frac{V_j p_j^2}{2\rho c^2} + \sum_{k=1}^{N}\frac{\beta_{jk}\rho S_{jk}h_{jk}v_{jk}e_- v_{jk}}{4}\right) \quad (27a)$$

$$\mathfrak{b} = \sum_{l=1}^{N_b}S_l v_l \mu_+ p_{j_l}. \quad (27b)$$

Here, $\mathfrak{h}_i$ is the discrete equivalent of the energy stored internally in the acoustic field—as such, it depends only on pressure values at the cells, and velocities at internal cell boundaries. The boundary term $\mathfrak{b}$ has been written in terms of the outward normal velocities v_l and the pressures p_{j_l} with which they are uniquely associated (the converse is not true if a cell possesses more than one boundary face, as might be needed, e.g., at domain corners). $\mathfrak{b}$ is not fully determined until numerical boundary conditions have been supplied.

B. Numerical Boundary Conditions

As a first step, it is convenient to write the normal boundary velocities $v_l^{n+1/2}$, which are interleaved in time with respect to pressure values p_j^n, in terms of an average of values $\bar{v}_l^n$ which are collocated in time with pressure values, as

$$v_l^{n+1/2} = \mu_+ \bar{v}_l^n. \tag{28}$$

At this point, one may immediately proceed to a discretization of the impedance boundary conditions (11):

$$\bar{v}_l = \sum_{m=1}^{M_l} \bar{v}_l^{(m)} \tag{29a}$$

$$\mu_+ p_{j_l} = L_l^{(m)} \delta_+ \bar{v}_l^{(m)} + R_l^{(m)} \mu_+ \bar{v}_l^{(m)} + \frac{1}{C_l^{(m)}} \mu_+ g_l^{(m)} \tag{29b}$$

$$\delta_+ g_l^{(m)} = \mu_+ \bar{v}_l^{(m)}. \tag{29c}$$

Here, the boundary admittance at the lth boundary face has been written as a parallel combination of M_l series RLC branches, as illustrated in Fig. 1; M_l need not be the same at each boundary face, allowing for more or less detailed modeling as needed.

C. Energy Balance and Numerical Stability Conditions

Examining the term $\mathfrak{b}$, using (29a), it may be rewritten as

$$\mathfrak{b} = \sum_{l=1}^{N_b} \sum_{m=1}^{M_l} S_l \mu_+ \bar{v}_l^{(m)} \mu_+ p_{j_l}. \tag{30}$$

Using (29b) and (29c), $\mathfrak{b}$ may be written as

$$\mathfrak{b} = \mathfrak{q} + \delta_+ \mathfrak{h}_b, \tag{31}$$

where

$$\mathfrak{q} = \sum_{l=1}^{N_b} \sum_{m=1}^{M_l} S_l R_l^{(m)} \left(\mu_+ \bar{v}_l^{(m)} \right)^2 \geq 0 \tag{32}$$

$$\mathfrak{h}_b = \frac{1}{2} \sum_{l=1}^{N_b} \sum_{m=1}^{M_l} S_l \left(L_l^{(m)} \left(\bar{v}_l^{(m)} \right)^2 + \frac{1}{C_l^{(m)}} \left(g_l^{(m)} \right)^2 \right) \geq 0. \tag{33}$$

The energy balance (26) may now be written as

$$\delta_+ \mathfrak{h} = -\mathfrak{q}, \tag{34}$$

where $\mathfrak{h} = \mathfrak{h}_i + \mathfrak{h}_b$. Because $\mathfrak{q}$ and $\mathfrak{h}_b$ are non-negative, dissipativity of the system as a whole, and thus numerical stability

follows from a non-negativity condition on the internal energy $\mathfrak{h}_i$. To find such a condition, use the identity (25) with the expression for $\mathfrak{h}_i$ from (27a), to give

$$\mathfrak{h}_i \geq \sum_{j=1}^{N} \left(\frac{V_j p_j^2}{2\rho c^2} - \sum_{k=1}^{N} \frac{\beta_{jk} \rho T_s^2 S_{jk} h_{jk} (\delta_- v_{jk})^2}{16} \right). \tag{35}$$

Using the scheme update for velocities at internal faces from (21b), this expression can be rewritten as

$$\mathfrak{h}_i \geq \sum_{j=1}^{N} \left(\frac{V_j p_j^2}{2\rho c^2} - \sum_{k=1}^{N} \frac{\beta_{jk} T_s^2 S_{jk} (p_k - p_j)^2}{16 \rho h_{jk}} \right), \tag{36}$$

which is a quadratic form in the cell pressures. Though it is possible to arrive at a non-negativity condition through eigenvalue analysis, a useful bound may be further obtained as

$$\mathfrak{h}_i \geq \sum_{j=1}^{N} p_j^2 \left(\frac{V_j}{2\rho c^2} - \sum_{k=1}^{N} \frac{\beta_{jk} T_s^2 S_{jk}}{4 \rho h_{jk}} \right). \tag{37}$$

For a given collection of cells Ω_j, then, with volumes V_j, adjoining internal faces S_{jk} and inter-cell distances h_{jk}, a non-negativity condition may be obtained locally as

$$\frac{1}{V_j} \sum_{k=1}^{N} \frac{\beta_{jk} c^2 T_s^2 S_{jk}}{2 h_{jk}} \leq 1 \quad \text{for} \quad j = 1, \ldots, N \tag{38}$$

This condition is also familiar as the stability condition for interior cells proposed by Botteldooren using a digital filter approach [2], although extensions to boundary cells and their associated frequency-independent impedance boundary conditions were not provided.

For a tiling of cubic cells, with a distance between cell centers of h, and using (17), such a condition reduces to $cT_s/h \leq 1/\sqrt{3}$ on the interior, which is the familiar von Neumann condition for seven-point FDTD schemes for the 3-D wave equation [29]. However, for a tiling of rhombic dodecahedral cells, using (18), the condition reduces to $cT_s/h \leq 1/\sqrt{3}$ on the interior, which is more strict than the von Neumann condition for the associated FDTD scheme over the interior, which is $cT_s/h \leq 1/\sqrt{2}$. More comments on this discrepancy appear in Section VII. Some strategies for fitting cells at boundaries that satisfy (38) can be found in [16].

D. Implementation Details

For implementation purposes, it helps to rewrite the FVTD scheme solely in terms of the scalar field Ψ and the boundary quantities $\bar{v}^{(m)}$ and $g^{(m)}$. Combining (22), (28) and (29a)–(29c), the update for Ψ_j becomes:

$$\Psi_j^+ = \left[2\Psi_j - \Psi_j^- + \frac{c^2 T_s^2}{V_j} \sum_{k=1}^{N} \frac{\beta_{jk} S_{jk}}{h_{jk}} (\Psi_k - \Psi_j) \right.$$

$$\left. - \frac{c^2 T_s^2}{2 V_j} \sum_{l=1}^{N_b} \sum_{m=1}^{M_l} \gamma_{jl} S_l \eta_l^{(m)} \left(\frac{2 L_l^{(m)} \bar{v}_l^{(m)}}{T_s} - \frac{g_l^{(m)}}{C_l^{(m)}} - \frac{\rho \Psi_j^-}{2 T_s} \right) \right] \Bigg/$$

$$\left[1 + \frac{\rho c^2 T_s}{4 V_j} \sum_{l=1}^{N_b} \sum_{m=1}^{M_l} \gamma_{jl} S_l \eta_l^{(m)} \right], \tag{39}$$

where $\Psi^\pm := e_\pm \Psi^{n+1/2}$, and g and $\bar{v}$ are defined at discrete time step n, where

$$\eta_l^{(m)} = \left(\frac{L_l^{(m)}}{T_s} + \frac{R_l^{(m)}}{2} + \frac{T_s}{4C_l^{(m)}} \right)^{-1}. \qquad (40)$$

This is followed by the updates for the boundary quantities $e_+\bar{v}_l^{(m)}$ and $e_+ g_l^{(m)}$:

$$e_+\bar{v}_l^{(m)} = \eta_l^{(m)} \left[\left(\frac{L_l^{(m)}}{T_s} - \frac{R_l^{(m)}}{2} - \frac{T_s}{4C_l^{(m)}} \right) \bar{v}_l^{(m)} \right.$$
$$\left. - \frac{g_l^{(m)}}{C_l^{(m)}} + \frac{\rho}{2T_s} \sum_{j=1}^{N} \gamma_{jl} \left(\Psi_j^+ - \Psi_j^- \right) \right] \qquad (41a)$$

$$e_+ g_l^{(m)} = \frac{T_s}{2} \left(e_+\bar{v}_l^{(m)} + \bar{v}_l^{(m)} \right) + g_l^{(m)}. \qquad (41b)$$

V. bASSIGNMENT OF BOUNDARY COEFFICIENTS

Assigning coefficients to approximate boundary admittances is deceptively difficult primarily due to difficulties in acquiring realistic broadband data. To produce the data below, a *transfer matrix model* (TMM) is used to compute admittances of layered wall structures [30], [31]. The TMM is based on analytical solutions of wave propagation across elements such as flexible panels, porous material layers, and air cavities.

A. Materials

Three layered wall structures and treatments that might be found in a typical room are shown in Fig. 6. The first two are based on a double-leaf gypsum wall with an 8.89 cm cavity. In the cavity is porous insulation defined by the Delany-Bazley-Miki model [30]. Material #1 is meant to approximate a double curtain hung in front of a wall using two 1 cm-thick porous layers. Material #2 is meant to approximate a porous treatment mounted in front of the gypsum wall, and Material #3 is a 10 cm-thick porous layer mounted to a thick panel, which might approximate soft materials such as seat cushions. For convenience the porous layers and gypsum panels are re-used in multiple structures. Specific material properties are reported in Table I.

B. Coefficient Estimation

Coefficients $L_l^{(m)}$, $R_l^{(m)}$, and $C_l^{(m)}$, are estimated such that deviation between the transfer matrix predictions and the admittance, as given in (10), is minimized. Minimization is done with the Nelder-Mead simplex method, and positivity of the coefficients is forced by specifying infinite error if coefficients are negative. Ensuring positivity of circuit element values is a guarantee of positive realness, and, in the numerical case, of passivity and numerical stability, as illustrated using energy techniques in the previous section. Error is otherwise measured by the Euclidean norm of differences between real and imaginary parts of the surface admittance. This is preferable to fitting magnitude and phase because it avoids wraparound ambiguity. To avoid over-emphasizing the fit at high frequencies, admittance data are computed with the TMM on exponentially spaced frequency points.
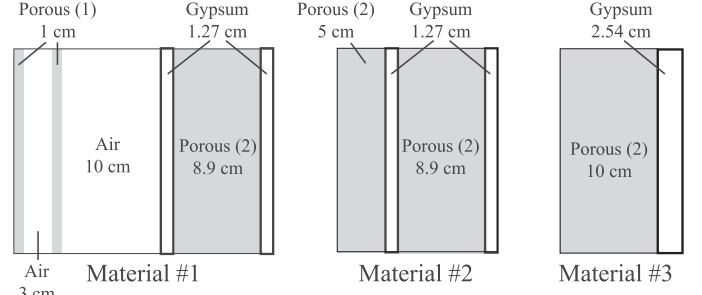

Fig. 6. Diagrams of wall structures used for computing data for boundary conditions. Components are porous layers, air cavities, and solid panels. Thickness are shown in the figure, and material properties of each component are given in Table I.

TABLE I
MATERIAL PROPERTIES OF WALL ELEMENTS USED
TO COMPUTE SURFACE ADMITTANCE

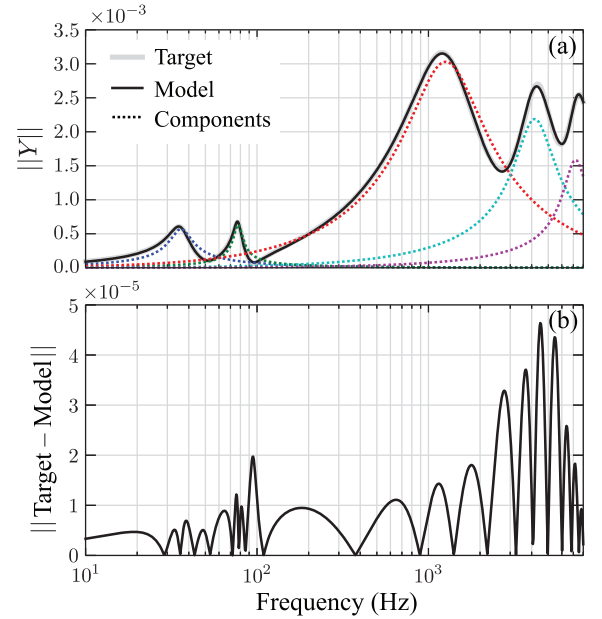|		
Gypsum Panels	Young's Modulus	1.47 GPa
	Loss Factor	0.4%
	Mass Density	1000 kg/m
Porous Layers	Flow Resistivity (1)	1300 Ns/m^4
	Flow Resistivity (2)	10^4 Ns/m^4
Air Cavities	Density	1.25 kg/m^3
	Sound Speed	340 m/s

Fig. 7. (a) Surface admittance predicted by the TMM (Target) for Material #2 with the LRC model fit including each component branch. (b) Deviation between the magnitudes of target and model.

To facilitate data fitting in moderate dimensions—15 to 27 dimensions in this case—the minimization uses a highly-informed initialization. An ad-hoc peak-finding algorithm is used to identify each resonance or peak in the data, approximate its height, and estimate its half-power bandwidth. This information is sufficient to specify approximate initial parameters for the admittance model. Since the minimization can only find local minima, several initializations are used with small perturbations added to the initial estimates of the coefficients. From multiple runs, the best fit is retained. Fig. 7 shows a typical data set and fit for the
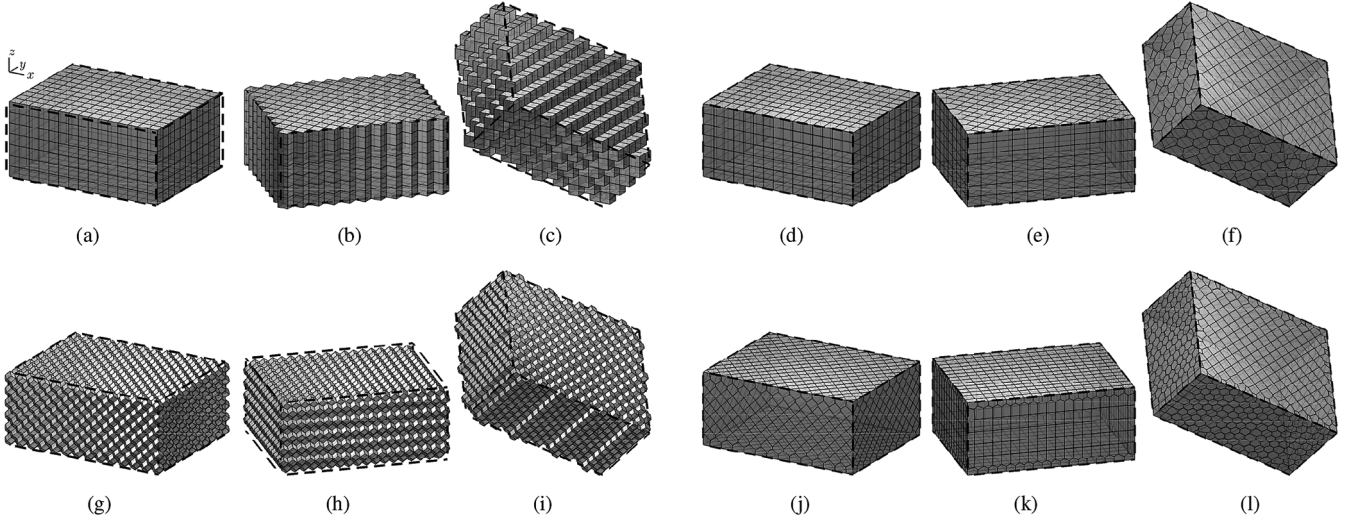
Fig. 8. Surface meshes of boundary faces after volumetric meshing of $4\sqrt{5}$ m $\times$ $4\sqrt{3}$ m $\times$ 4 m box centered about the origin under various rotations. The meshings use staircase approximations with cubic cells and rhombic dodecahedral cells from the FCC grid. Meshings using fitted cells are adapted from the staircase meshings, and thus, only differ from staircase meshes for cells located near the boundaries of the box domain. The code "R0" denotes no rotation, so that the box is aligned with the principal axes, the code "R1" denotes a 45° rotation about the z-axis, and the code "R2" denotes successive 45° rotations about the z- and y-axes (in that order). In each case, the thick dashed line denotes the ideal rotated box domain. In this figure, the inter-cell distance for interior adjacent cubic and rhombic dodecahedral cells was set to $h = cT_s\sqrt{3} \approx 59$ cm, where $1/T_s = 1000$ Hz and $c = 340$ m/s. (a) Cubic, staircase, R0 (b) Cubic, staircase, R1 (c) Cubic, staircase, R2 (d) Cubic, fitted, R0 (e) Cubic, fitted, R1 (f) Cubic, fitted, R2 (g) FCC, staircase, R0 (h) FCC, staircase, R1 (i) FCC, staircase, R2 (j) FCC, fitted, R0 (k) FCC, fitted, R1 (l) FCC, fitted, R2.

TABLE II
TABLE OF LRC COEFFICIENTS FOR THE MODELS FIT TO THE TRANSFER MATRIX PREDICTIONS FOR THREE MATERIALS IN FIG. 6

L^m	R^m	C^m
Material #1		
24.4272	1672.6264	8.4126×10^{-7}
23.2179	1210.5657	1.8279×10^{-7}
9.6630×10^{-2}	39.3922	8.4863×10^{-7}
9.4285×10^{-2}	35.8868	9.3606×10^{-8}
9.4588×10^{-2}	55.0224	3.3616×10^{-8}
9.8014×10^{-2}	76.1128	1.6608×10^{-8}
1.0520×10^{-1}	54.2331	9.2427×10^{-9}
1.0114×10^{-1}	58.0354	6.4229×10^{-9}
8.8486×10^{-2}	99.5043	5.3150×10^{-9}
Material #2		
26.0297	1749.91	7.49563×10^{-7}
26.6955	1583.26	1.57614×10^{-7}
4.1593×10^{-2}	330.129	3.83857×10^{-7}
3.2549×10^{-2}	457.115	4.47654×10^{-8}
4.2137×10^{-2}	629.982	1.15506×10^{-8}
Material #3		
22.7431	750.5833	2.1842×10^{-7}
8.1499×10^{-2}	336.6442	7.3053×10^{-7}
6.7680×10^{-2}	491.0421	7.8999×10^{-8}
6.4599×10^{-2}	676.5088	2.6469×10^{-8}
1.6493×10^{-2}	493.5131	3.4710×10^{-8}
7.1131×10^{-3}	60.0617	2.3215×10^{-8}

admittance of Material #2, and coefficients estimated for all of the materials are reported in Table II.

VI. SIMULATIONS

A. Rotated Box Under Perfectly Reflective Conditions

A useful test case, for which some analytic solutions are available, is that of a rectangular box-shaped region. Here, to illustrate the effects of staircase approximations, and the use of fitted cells, the box will be rotated with respect to the principal axes defining the grid of cells, assumed uniform over the interior of the domain. The box is of dimensions L_x, L_y, L_z, lying, when unrotated, between $-L_x/2 \leq x \leq L_x/2$, $-L_y/2 \leq y \leq L_y/2$ and $-L_z/ \leq z \leq L_z/2$. Under perfectly reflective conditions (i.e., for $v_\perp = 0$ along all boundaries), the modal frequencies of the box are given by

$$f_{q_x,q_y,q_z} = \frac{c}{2}\sqrt{\frac{q_x^2}{L_x^2} + \frac{q_y^2}{L_y^2} + \frac{q_z^2}{L_z^2}} \quad q_x, q_y, q_z = 0, 1, \ldots \quad (42)$$

For this test, a box of size $4\sqrt{5}$ m $\times$ $4\sqrt{3}$ m $\times$ 4 m was meshed under three rotations (R0,R1,R2) using cubic and rhombic dodecahedral cells, with staircase and fitted approximations at the boundaries, and for various cell sizes, as described and illustrated in Fig. 8. Grid spacings for interior cells were set as $h = cT_s\sqrt{3}$, where $c = 340$ m/s and $1/T_s = 1$ kHz, 2 kHz, ..., 10 kHz. Meshings were carried out such that condition (38) was satisfied at each cell. The percent errors in the volumes and surfaces areas of these meshing are displayed in Fig. 9. It can be seen that for staircase approximations, the volume error remains low, but similarly to the example illustrated in Fig. 4, the surface area does not improve in the limit of small cells sizes—aside from the special case labelled 'R0', which represents the box unrotated with respect to a Cartesian grid (this case converges). Meanwhile for the fitted meshes, errors for surface area and volume approximations remained below 1e-9% (not shown).

The modal frequencies from these discrete models were obtained using an eigenvalue analysis of the two-step update matrix for each scheme. Fig. 10 shows the first four modal frequencies for staircase and fitted cell approximations to the box under the three rotations (R0,R1,R2) illustrated and described in
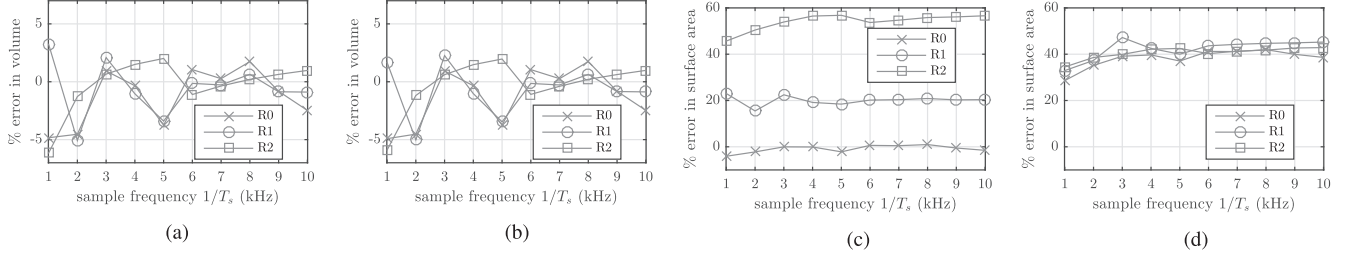
Fig. 9. Percent error in surface areas and volumes of staircase meshings under rotations (R0,R1,R2) defined in Fig. 8. (a) Volume % errors, cubic grid (b) Volume % errors, FCC grid (c) Surface area % errors, cubic grid (d) Surface area % errors, FCC grid.
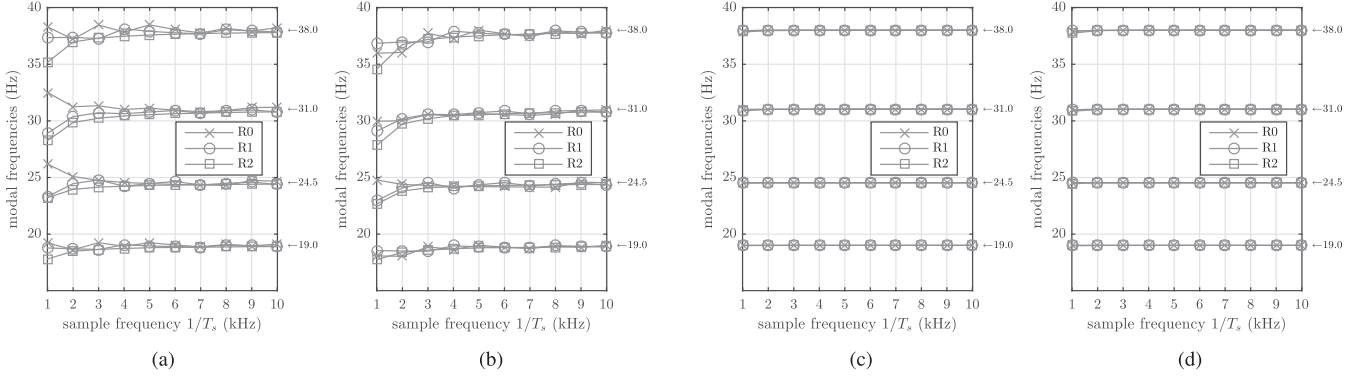

Fig. 10. Frequencies of first four modes from simulated rotated box under Neumann boundary conditions under three rotations (R0,R1,R2), as well as analytical modal frequencies marked on right. (a) Cubic grid, staircase (b) FCC grid, staircase (c) Cubic grid, fitted (d) FCC grid, fitted.

Fig. 8. It can be seen from Fig. 10 that close matches to the analytical frequencies are obtained using fitted cells, while staircase approximations only give good matches in the limit of small cell sizes (or high sample rates, for a fixed Courant number).

B. Rotated Box Under Resistive Termination at Opposing Faces

In order to examine the effects of staircase approximations on room mode decay times more general impedance terminations should be employed, but in that case the wave equation is not separable and thus modal frequencies are not available in closed form. There is, however, one case for which a family of modes is separable. Consider a box under resistive boundary conditions with admittance $Y = \alpha/\rho c$ over the two faces with $x = \pm L_x/2$, and $Y = 0$ over all other faces, when unrotated. Under such conditions, one axial family of modes is separable, with the exact frequencies f_q and T_{60} decay times τ_q:

$$ f_q = \frac{cq}{2L_x} \quad \tau_q = \frac{6L_x \ln(10)}{c \ln\left(\left|\frac{1+\alpha}{1-\alpha}\right|\right)} \quad q = 1, 2, \dots \quad (43) $$

As in the previous example, the box dimensions and rotations employed for this test are illustrated and described in Fig. 8. Impedances for boundary faces associated with opposing faces of the box, along the longest dimension, were set with $c = 340 \, \text{m/s}$ and $\alpha = 0.05$, resulting in an ideal T_{60} of 3.63 seconds for the family of modes under consideration. Approximated T_{60} times for the first two modes in this family were extracted from an interior-eigenvalue analysis and the associated errors are plotted in Fig. 11. It can be seen that T_{60} times are accurately reproduced with fitted meshings; meanwhile, the staircase approximations exhibit significant errors that do not disappear in the

limit of small cell sizes, aside from the special case labelled 'R0'. In effect, the resulting T_{60} times are under-approximated for the staircase grids because surface areas, and thus absorptive surfaces, are over-approximated. Although, there seems to be no simple relationship between meshing errors and T_{60} errors (compare Figs. 9 and 11), which would suggest that one cannot simply modify absorption parameters at walls to compensate for meshing errors and expect to simulate accurate T_{60} times.

Finally, it is worth mentioning that standard frequency domain analyses [14] of these schemes would indicate that numerical dispersion errors are insignificant at the highest sample rates considered here; for the cubic scheme with a 10 kHz sample rate and $\lambda = \sqrt{1/3}$, dispersion errors are less than 0.0005% and 0.02% for the 19 Hz and 38 Hz modes respectively. It is therefore safe to say that dispersion error is not a factor in the exhibited T_{60} errors. More will be said about this in Section VII in regards to pseudospectral approaches.

With regards to other FDTD methods, it would be insightful to conduct the tests in Section VI with popular 27-point interpolated schemes [14]. However, boundary updates that apply to complex geometries have yet to be formulated for such schemes; applying the few special case boundary updates that are available [14] to a rotated box would ultimately amount to another form of staircase approximation, for which gross T_{60} errors would likely be observed, at least for the test case in Section VI-B. Another comparison left out here is with digital waveguide mesh (DWM) models that employ "1-D" boundary terminations [5]. However, it has been found that such models have equivalent finite volume formulations, and while they are passive (and thus, stable) by construction, the resulting meshings demonstrate severe staircasing effects, but more importantly, consistency is not guaranteed when wall admittances are non-zero [16].
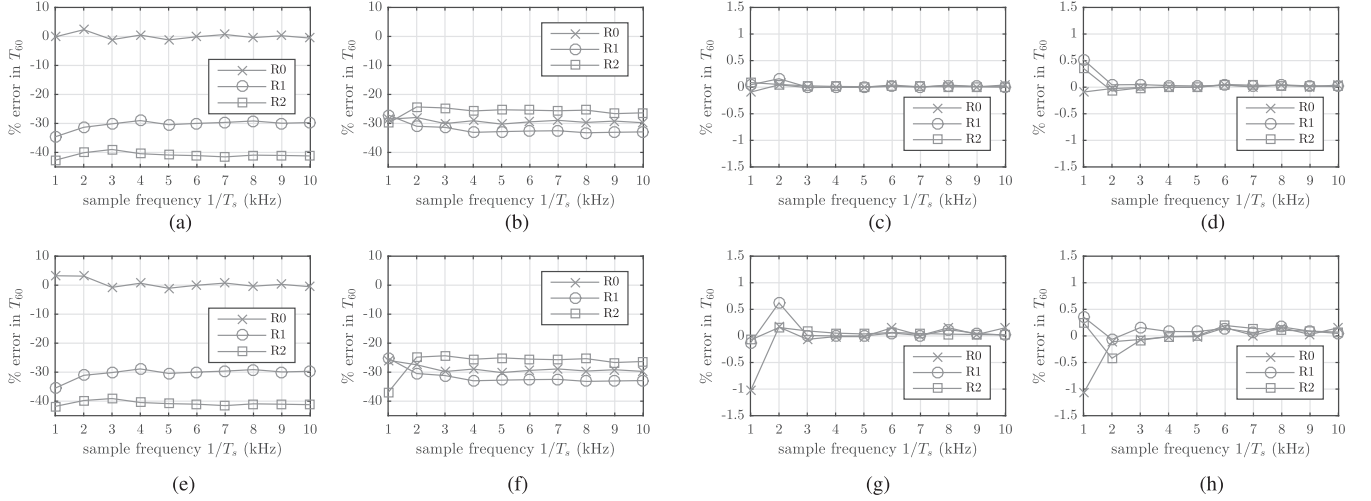
Fig. 11. Percent error in T_{60} times of two modes from simulated rotated box under resistive boundary conditions ($\alpha = 0.05$) and three rotations (R0,R1,R2) with respect to the cubic and FCC grids. (a) Cubic, staircase, 19.0 Hz mode (b) FCC, staircase, 19.0 Hz mode (c) Cubic, fitted, 19.0 Hz mode (d) FCC, fitted, 19.0 Hz mode (e) Cubic, staircase, 38.0 Hz mode (f) FCC, staircase, 38.0 Hz mode (g) Cubic, fitted, 38.0 Hz mode (h) FCC, fitted, 38.0 Hz mode.
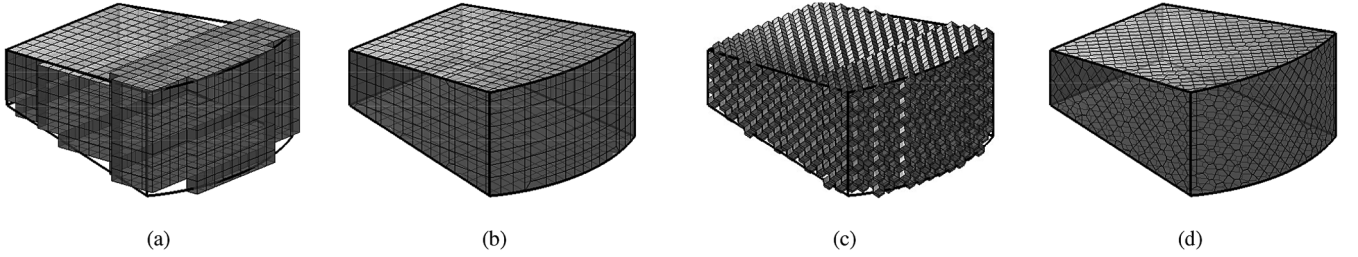

Fig. 12. Boundary surface meshes from volumetric meshing of fan-shaped domain, using staircase and fitted approximations derived from cubic and FCC grids, with $h = cT_s/\lambda$, where $1/T_s = 1000$ Hz and $\lambda = \sqrt{1/3}$ for the cubic grid and $\lambda = 0.7$ for the FCC grid. (a) Staircase, cubic (b) Fitted, cubic (c) Staircase, FCC (d) Fitted, FCC.
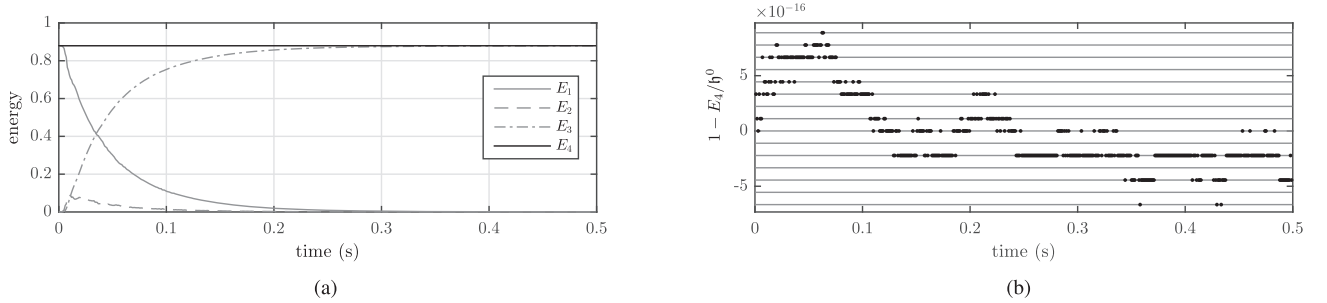

Fig. 13. Demonstration of numerical energy conservation with fitted mesh based on rhombic dodecahedral cells, with $\lambda = 0.7$ and $1/T_s = 1$ kHz. (a) Plot of energetic quantities over time, where $E_1 = \mathfrak{h}_i^n$, $E_2 = \mathfrak{h}_b^n$, $E_3 = \sum_{\bar{n}=0}^{n-1} T_s \mathfrak{q}^{\bar{n}+1/2}$ and $E_4 = E_1 + E_2 + E_3$. Note that E_3 is the cumulative sum of power dissipated. (b) Energy conservation, taking into account cumulative sum of boundary losses. Gray lines denote integer multiples of machine epsilon (2^{-53}).

C. A Complex Geometry Under General Variable Impedance Conditions

The following numerical experiments serve to demonstrate the behavior of the finite volume scheme with general impedance boundaries on a more complex geometry. Two features will be demonstrated here: energy conservation to machine accuracy and an invariance with respect to rotation and choice of the grid when fitted cells are employed.

For this test, a theatre-shaped room was designed with five flat faces and one curved face (piecewise-linear), and the room was meshed under the three rotations (R0,R1,R2) using cubic and rhombic dodecahedral cells with staircase and fitted approximations. The domain of interest and example meshings are shown in Fig. 12. General impedance boundaries with up to nine RLC branches were associated to each wall; Materials #1 and #2 were associated to the curved and largest flat face, respectively, and Material #3 was attributed to the remaining four flat faces. The

total volume of the room was 325 m^3 and the grid spacings for interior cells were chosen to be $h = cT_s/\lambda$ with $\lambda = \sqrt{1/3}$ for cubic cells, and $\lambda = 0.7$ for rhombic dodecahedral cells, with $1/T_s$ set to 4 kHz or 8 kHz, and $c = 340$ m/s and $\rho = 1.25$ kg/m^3. Meshing errors (volume, surface area) for fitted meshes were on the order of 1e-9%, while staircase meshes demonstrated errors in surface area between 15% and 50%. The initial conditions for this problem were $\partial_t \Psi(\mathbf{x}, 0) = 0$ and $\Psi(\mathbf{x}, 0)$ equal to a spatial Gaussian centered about $(x, y, z) = (-1, 3, 0.5)$ m with a variance of $(0.4\,\text{m})^2$. Snapshots of a simulation can be seen in Fig. 14.

Conservation of numerical energy, taking into account accumulated losses, can be demonstrated in the simulation, and is a useful debugging tool for such schemes. This is done by calculating the quantities $\mathfrak{h}_i$, $\mathfrak{h}_b$ and $\mathfrak{q}$ in the run-time loop, as seen in Fig. 13. The numerical energy balance is conserved to machine accuracy, and in particular, the variations in energy appear in discrete steps of machine epsilon.
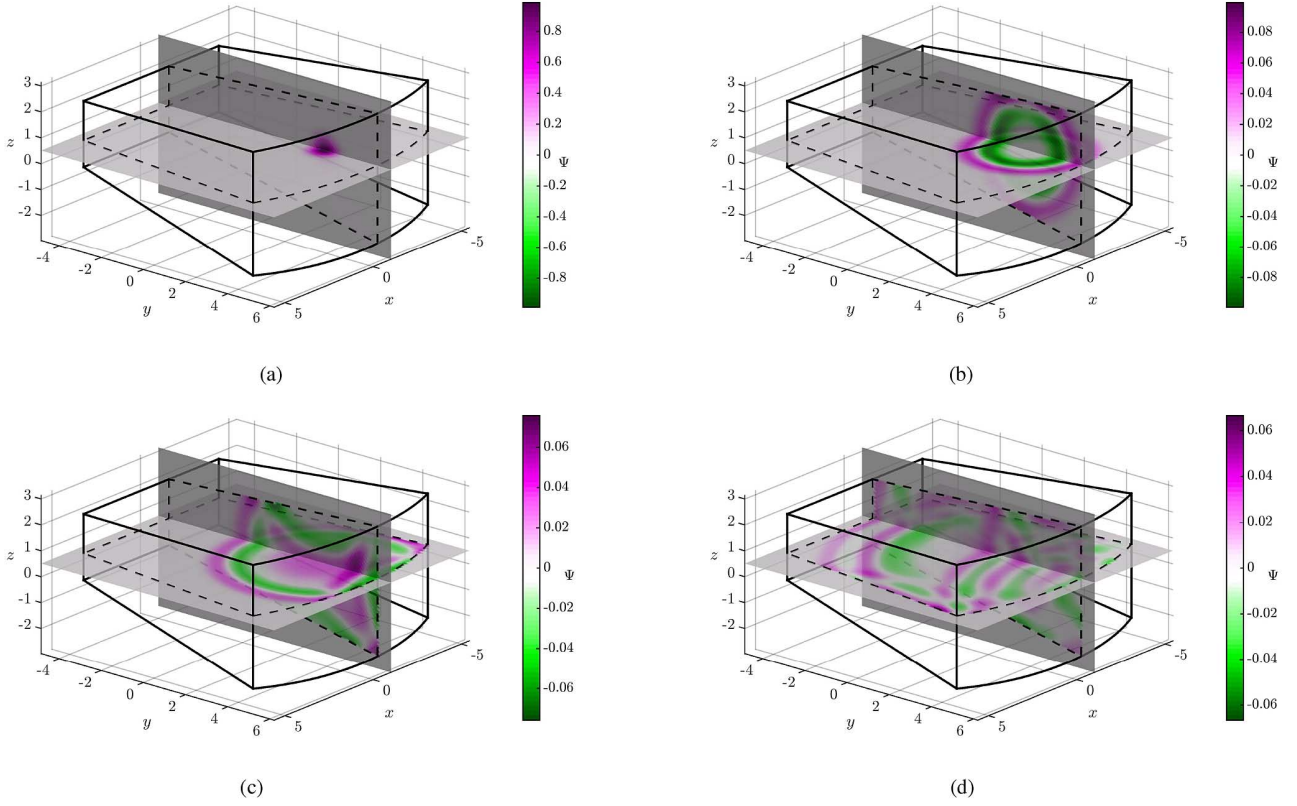
(a)

(b)

(c)

(d)

Fig. 14. Snapshots for test problem described in Section 6.3 on a fitted mesh derived from the FCC grid with $\lambda = 0.7$ and $1/T_s = 4$ kHz. Spatial axes are in units of metres. (a) $t = 0$, (b) $t = 5$ ms, (c) $t = 10$ ms, (d) $t = 20$ ms.
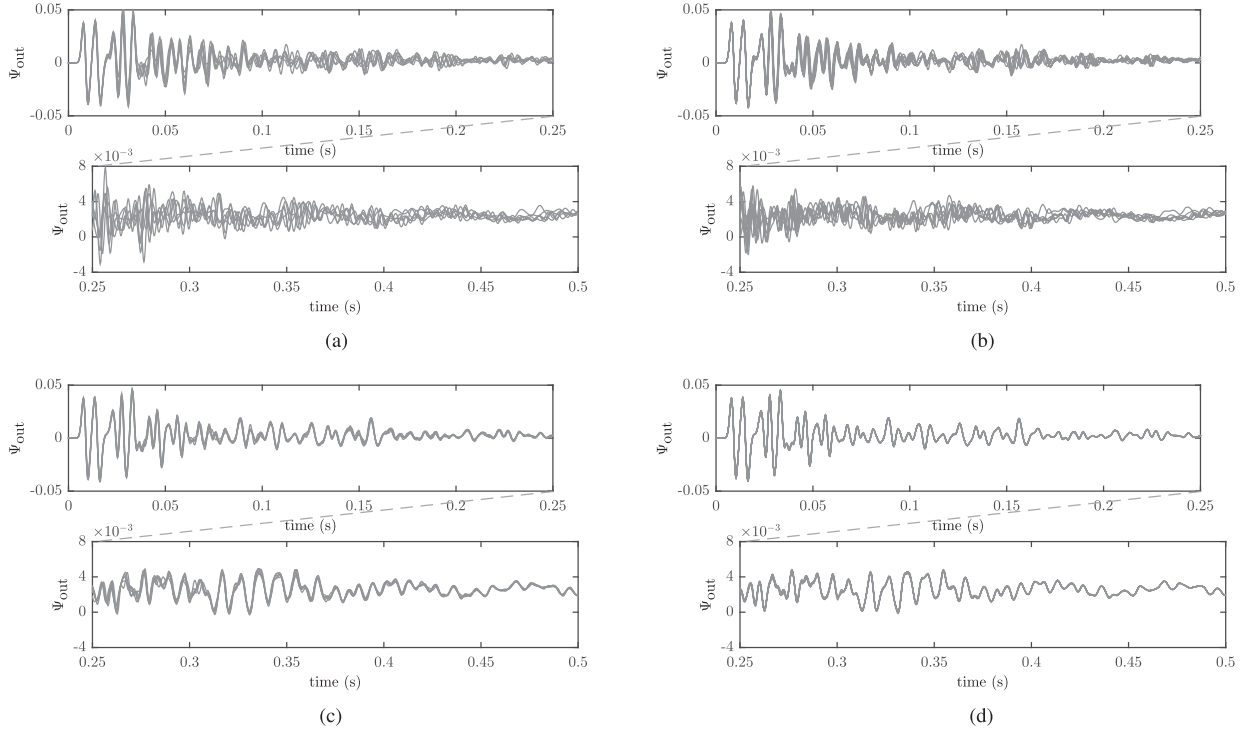

(a)

(b)

(c)

(d)

Fig. 15. Plots of Ψ_{out} for staircase and fitted approximations at various sample rates. The duration $t \in [0, 0.5 \text{ s}]$ is split in half to show detail. Six curves are overlaid within each plot; these pertaining to cubic and rhombic dodecahedral cells each under the three rotations: R0, R1, R2. (a) Staircase approximations, $1/T_s = 4$ kHz, (b) Staircase approximations, $1/T_s = 8$ kHz, (c) Fitted approximations, $1/T_s = 4$ kHz, (d) Fitted approximations, $1/T_s = 8$ kHz.

When using fitted cells, the finite volume solution can provide for a more reliable numerical solution than staircase methods, as it remains relatively invariant to the choice of cell and rotation of the grid. In regards to this test case, the numerical so-

lution read at the origin (Ψ_{out}) is shown as a function of time in Fig. 15, wherein each subfigure (Figs. 15(a)–(d)) pertains to either a fitted or staircase approximation at a given sample rate (4 kHz or 8 kHz). Overlaid within each plot are six time se-

ries, which pertain to the simulations with cubic and rhombic dodecahedral cells each under the three rotations of the domain (R0,R1,R2).

Considering the entire duration $t \in [0, 0.05]$ s, it can be seen in Fig. 15, that the staircase approximations demonstrate a large variance with respect to the choice of cell and rotation of domain, particularly after the arrival of the first few early reflections, and this variance does not appear to decrease with T_s. However, considering only the epoch ($t \in [0, 0.05]$ s) in staircase approximations, it can be seen that the direct sound ($t < 0.01$ s) is rendered accurately (due to consistency on the interior) and interestingly, the first few early reflections ($t \in [0.01, 0.05]$ s) are also well rendered. Looking at the fitted approximations, a low variance with respect to rotation and cell choice is demonstrated, and this variance decreases with T_s, suggesting that the fitted approximations converge to a unique (true) solution; in contrast, it is clear from the analysis of the rotated box that staircase approximations cannot converge to the true solution, as the total surface area (and thus the T_{60}, at least for certain modes) will be incorrect regardless of the degree of mesh refinement.

VII. CONCLUDING REMARKS AND PERSPECTIVES

The finite volume time domain approach to room acoustics simulation is a flexible one, and, as mentioned previously, generalizes certain FDTD methods, allowing for stability analysis in the unstructured case through energy methods. This permits accurate fitting of cells at the room boundary; the effect of such fitting has been shown here to produce minor improvements, with little additional computational cost, in the accuracy of room mode frequencies, and major improvements in terms of computed mode decay times. Indeed, under a staircase approximation, computed T_{60} times under such a staircase approximation can deviate by as much as 40% from theoretical values, at least for the special case considered in Section II-B—and furthermore, the decay times do not converge to theoretical values even in the limit of small cell size (or high sample rate, for a fixed Courant number) as dispersion errors become insignificant. There remain several unresolved questions, all of which constitute avenues for further research.

The problem of choosing an arrangement of cells (or meshing) to cover a 3D region is a longstanding one, particularly within nonlinear computational fluid dynamics, where, in order to resolve viscothermal boundary layers, it is desirable to have fine meshing at the boundary of the region of interest. In linear room acoustics, the problem is somewhat simplified, and indeed, the best choice of meshing would appear to be one which is as uniform as possible over the problem interior. At the boundary, however, it has been shown here that, at least in the finite volume setting, accurate fitting of boundary cells is a necessity for accurate T_{60} simulation in the general case. This leads to a meshing problem over the room boundary for which there are many possible solutions. It would be of great interest to find an optimal strategy for the meshing step, and one that is computationally efficient enough to handle potentially very large regions.

Sufficient stability conditions for a completely unstructured arrangement of cells, and under general locally-reactive impedance boundary conditions, have been illustrated here. Through energy analysis techniques, the stability problem can be neatly separated into an analysis of the resulting scheme over the interior and over the boundary. Furthermore, the conditions given in (38) can be verified locally, including at irregular fitted cells adjacent to a boundary. An interesting observation is that, even for regular cell arrangements on the interior, in the cases that FVTD reduces to FDTD, the conditions do not always coincide with known von Neumann conditions for the interior scheme. For cubic cells, the condition is equivalent to the stability condition arising from von Neumann analysis, but this is not the case for rhombic dodecahedral cells (or even hexagonal cells in the 2D case). For meshes based on the latter two cells, it is possible to operate beyond the passivity limit (38) (as conducted in Section VI-C) into the regime where dispersion error is minimized, and stability conditions can be obtained through an eigenvalue analysis of quadratic forms like (36). An area of future research will be to establish locally verifiable bounds that are more relaxed than (38) for FCC and hexagonal grids.

It is also worth pointing out that domain decomposition approaches based on modal [32] and pseudospectral methods [33] usually fall under the category of staircase approximations, as they rely on dividing up an arbitrary domain into box-shaped partitions in order to take advantage of the FFT algorithm. While such methods may provide little to no dispersion error, the same types of modal and T_{60} errors due to staircasing effects may be a concern, even if the wave equation is very accurately solved on the interior. Pseudospectral methods with conformal mappings have been proposed to address such staircasing issues [34].

Finally, locally reactive impedance boundary conditions have been approximated by a particular sub-class of positive real functions which can be written as a parallel combination of series RLC branches. Though such a structure leads to convenience in terms of optimization to measured or theoretical impedance curves, it is not the most general class of positive real functions. It would thus be of great utility to extend the optimization here to the entire space of positive real functions. The extension to the case of non-locally reactive boundary conditions remains open.

REFERENCES

[1] O. Chiba, T. Kashiwa, H. Shimoda, S. Kagami, and I. Fukai, "Analysis of sound fields in three dimensional space by the time-dependent finite-difference method based on the leap frog algorithm," *J. Acoust. Soc. Jpn.(J)*, no. 49, pp. 551–562, 1993.

[2] D. Botteldooren, "Acoustical finite-difference time-domain simulation in a quasi-Cartesian grid," *J. Acoust. Soc. Amer.*, vol. 95, no. 5, pp. 2313–2319, 1994.

[3] L. Savioja, T. Rinne, and T. Takala, "Simulation of room acoustics with a 3-D finite-difference mesh," in *Proc. Int. Comp. Music Conf.*, Århus, Denmark, Sep. 1994, pp. 463–466.

[4] G. Campos and D. Howard, "On the computational efficiency of different waveguide mesh topologies for room acoustic simulation," *IEEE Trans. Speech Audio Process.*, vol. 13, no. 5, pp. 1063–1072, Sep. 2005.

[5] D. Murphy, A. Kelloniemi, J. Mullen, and S. Shelley, "Acoustic modelling using the digital waveguide mesh," *IEEE Signal Process. Mag.*, vol. 24, no. 2, pp. 55–66, Mar. 2007.

[6] R. Leveque, *Finite Volume Methods for Hyperbolic Problems*. Cambridge, U.K.: Cambridge Univ. Press, 2002.

[7] V. Shankar, W. F. Hall, and A. H. Mohammadian, "A time-domain differential solver for electromagnetic scattering problems," *Proc. IEEE*, vol. 77, no. 5, pp. 709–721, May 1989.

[8] S. Bilbao, "Modeling of complex geometries and boundary conditions in finite difference/finite volume time domain room acoustics simulation," *IEEE Trans. Audio Speech Lang. Process.*, vol. 21, no. 7, pp. 1524–1533, Jul. 2013.

[9] J. Allen and D. Berkley, "Image method for efficiently simulating small-room acoustics," *J. Acoust. Soc. Amer.*, vol. 66, no. 4, pp. 943–950, 1979.

[10] J. Strikwerda, *Finite Difference Schemes and Partial Differential Equations*. Pacific Grove, CA, USA: Wadsworth and Brooks/Cole Advanced Books and Software, 1989.

[11] B. Gustafsson, H.-O. Kreiss, and J. Oliger, *Time Dependent Problems and Difference Methods*. New York, NY, USA: Wiley, 1995.

[12] B. Gustaffson, H.-O. Kreiss, and A. Sundstrom, "Stability theory of difference approximations for mixed initial boundary value problems. II," *Math. Comput.*, vol. 26, no. 119, pp. 649–686, 1972.

[13] K. Kowalczyk and M. van Walstijn, "Modeling frequency-dependent boundaries as digital impedance filters in FDTD and K-DWM room acoustics simulations," *J. Audio Eng. Soc.*, vol. 56, no. 7/8, pp. 569–583, 2008.

[14] K. Kowalczyk and M. van Walstijn, "Room acoustics simulation using 3-D compact explicit FDTD schemes," *IEEE Trans. Audio, Speech, Lang. Process.*, vol. 19, no. 1, pp. 34–46, Jan. 2011.

[15] J. Botts and L. Savioja, "Spectral and pseudospectral properties of finite difference models used in audio and room acoustics," *IEEE/ACM Trans. Audio, Speech, Lang. Process.*, vol. 22, no. 9, pp. 1403–1412, Sep. 2014.

[16] B. Hamilton, "Finite volume perspectives on finite difference schemes, and boundary formulations for wave simulation," in *Proc. Digital Audio Effects (DAFx)*, Erlangen, Germany, Sep. 2014.

[17] J. Sheaffer, B. M. Fazenda, D. T. Murphy, and J. A. S. Angus, "A simple multiband approach for solving frequency dependent problems in numerical time domain methods," *Proc. Forum Acusticum*, pp. 269–274, 2011.

[18] M. Hornikx, Y. Smyrnowa, T. van Renterghem, C. Cheal, and J. Kang, "Acoustic simulation tools for urban streets, squares and road-side courtyards integrating vegetation," 2012, FP7 HOSANNA Deliverable 5.3.

[19] B. Hamilton and C. J. Webb, "Room acoustics modelling using GPU-accelerated finite difference, and finite volume methods on a face-centered cubic grid," in *Proc. Digital Audio Effects (DAFx)*, Maynooth, Ireland, Sep. 2013, pp. 336–343.

[20] P. Morse and U. Ingard, *Theoretical Acoustics*. Princeton, NJ, USA: Princeton Univ. Press, 1968.

[21] C. J. Webb and S. Bilbao, "Computing room acoustics with CUDA - 3D FDTD schemes with boundary losses and viscosity," in *Proc. IEEE Int. Conf. Acoust., Speech, Signal Process.*, 2011, pp. 317–320.

[22] B. Hamilton, S. Bilbao, and C. J. Webb, "Improved finite difference schemes for a 3-D viscothermal wave equation on a GPU," in *Proc. Forum Acusticum*, Krakow, Poland, 2014.

[23] H. Kuttruff, *Room Acoustics*, Fourth edition ed. New York, NY, USA: Taylor and Francis, 2000.

[24] L. Weinberg, *Network Analysis and Synthesis*. New York, NY, USA: McGraw-Hill, 1962.

[25] O. Brune, "Synthesis of a finite two-terminal network whose driving-point impedance is a prescribed function of frequency," Ph.D. dissertation, Mass. Inst. of Technol., Cambridge, MA, USA, 1931.

[26] R. Bott and R. Duffin, "Impedance synthesis without use of transformers," *J. Appl. Phys.*, vol. 20, no. 8, p. 816, 1949.

[27] M. van Valkenburg, *Network Analysis*. New York, NY, USA: Dover, 1975.

[28] D. Botteldooren, "Finite-difference time-domain simulation of low-frequency room acoustic problems," *J. Acoust. Soc. Amer.*, vol. 98, no. 6, pp. 3302–3308, 1995.

[29] G. E. Forsythe and W. R. Wasow, *Finite-Difference Methods for Partial Differential Equations*. New York, NY, USA: Wiley, 1960.

[30] J. Allard and N. Atalla, *Propagation of Sound in Porous Media: Modelling Sound Absorbing Materials*. New York, NY, USA: Wiley, 2009.

[31] M. L. Munjal, *Acoustics of Ducts and Mufflers*. New York, NY, USA: Wiley, 2014.

[32] N. Raghuvanshi, R. Narain, and M. C. Lin, "Efficient and accurate sound propagation using adaptive rectangular decomposition," *IEEE Trans. Vis. Comput. Graphics*, vol. 15, no. 5, pp. 789–801, Sep.-Oct. 2009.

[33] M. Hornikx, W. De Roeck, and W. Desmet, "A multi-domain Fourier pseudospectral time-domain method for the linearized Euler equations," *J. Comp. Phys.*, vol. 231, no. 14, pp. 4759–4774, 2012.

[34] M. Hornikx and D. Steeghs, "Acoustic propagation modeled by the curvilinear Fourier pseudospectral time-domain method," *Proc. Meetings Acoust.*, vol. 19, p. 015121, 2013, Acoustical Society of America.

Stefan Bilbao (B.A. Physics, Harvard, 1992 MSc., Ph.D. electrical engineering, Stanford, 1996 and 2001 respectively) is currently a Reader in the Acoustics and Audio Group at the University of Edinburgh, and was previously a Lecturer at the Sonic Arts Research Centre, at the Queen's University Belfast, and a Research Associate at the Stanford Space Telecommunications and Radioscience Laboratories. He is currently the leader of the NESS project (Next Generation Sound Synthesis), funded by the European Research Council, and running jointly between the Acoustics and Audio Group and the Edinburgh Parallel Computing Centre at the University of Edinburgh between 2012 and 2017.

Brian Hamilton received B.Eng. (Hons) and M.Eng. degrees in electrical engineering from McGill University in Montréal, QC, Canada, in 2009 and 2012, respectively. He is currently a Ph.D. student in the Acoustics and Audio group at the University of Edinburgh. His focus of research is finite difference and finite volume methods for 3D room acoustics simulations.

Jonathan Botts received a B.S. degree in physics and mathematics from Drake University in 2008 He received M.S. and Ph.D. degrees from Rensselaer Polytechnic Institute (RPI) in Architectural Acoustics in 2009 and 2012, respectively. From 2012 to 2014 he was a Postdoctoral Researcher in the Department of Media Technology at Aalto University in Espoo, Finland. He is currently a Postdoctoral Researcher at RPI. His research interests include numerical modeling and data analysis.

Lauri Savioja (M'00–SM'08) received the degrees of M.Sc., and the Doctor of Science in technology, from the Helsinki University of Technology (TKK), Espoo, Finland, in 1991 and 1999, respectively. In both degrees, he majored in computer science, and the topic of his doctoral thesis was room acoustic modeling. He was with the TKK Laboratory of Telecommunications Software and Multimedia as a Researcher, Lecturer, and Professor from 1995 till the formation of Aalto University where he currently works as a Professor and the Head of the Department of Media Technology. His research interests include room acoustics, virtual reality, and parallel computation. Prof. Savioja is a fellow of the Audio Engineering Society (AES), and a life member of the Acoustical Society of Finland. From 2010 to 2014 he was an Associate Editor of the IEEE Transactions on Audio, Speech, and Language Processing.